Available online at www.sciencedirect.com
ScienceDirect
Trans. Nonferrous Met. Soc. China 32(2022) 2609−2619
Transactions of Nonferrous Metals Society of China
www.tnmsc.cn

In-situ synchrotron X-ray diffraction investigation on deformation behavior of Nb/NiTi composite during pre-straining process

Shun GUO[1], Hui-hui ZHANG[1], Min-kyung KWAK[2], Wang DING[1], Guang-lei LIU[1], Wen MA[1,3], Hai-xia LIU[1], Qing-kun MENG[4], Xin-qing ZHAO[5]

1. School of Materials Science and Engineering, Jiangsu University, Zhenjiang 212013, China;
2. Department of Materials Science and Engineering, Seoul National University, Seoul 08826, Korea;
3. Youke Publishing Co., Ltd., Grinm Group Co., Ltd., Beijing 100088, China;
4. School of Materials Science and Engineering, China University of Mining and Technology, Xuzhou 221116, China;
5. School of Materials Science and Engineering, Beihang University, Beijing 100191, China

Received 31 July 2021; accepted 29 December 2021

Abstract: The mechanisms responsible for deformation behavior in Nb/NiTi composite during pre-straining were investigated systematically using in-situ synchrotron X-ray diffraction, transmission electron microscopy and tensile test. It is shown that upon loading, the composite experiences elastic elongation and slight plastic deformation of $B19'$, $B2$ and β-Nb phases, together with the forward stress-induced martensitic (SIM) transformation from $B2$ to $B19'$. Upon unloading, the deformation mechanisms of the composite mainly involve elastic recovery of $B19'$, $B2$ and β-Nb phases, compression deformation of β-Nb phase and incomplete $B19'\rightarrow B2$ reverse SIM transformation. In the tensile loading−unloading procedure, besides the inherent elastic deformation and SIM transformation, the (001) compound twins in $B19'$ martensite can also be conducive to the elastic deformation occurring in $B19'$-phase of the composite. Therefore, this composite can exhibit a large recoverable strain after unloading owing to the elastic deformation, and the partially reversible and consecutive SIM transformation together with the (001) compound twins.

Key words: Nb/NiTi composite; near-linear deformation behavior; large recoverable strain; martensitic transformation

1 Introduction

With the increase of the attention to health, people's demand for biomedical materials is increasing progressively [1−3]. At the same time, the increasingly strict requirements are proposed for the performance of biomedical materials. For some certain biomedical devices (e.g. self-expansible stents, orthopedic sensor clips and temporary orthopedic implants), biocompatibility, linear elasticity and recoverable strain are key performance indicators [4−7]. Therefore, the design and research on the materials with a superior combination of good biocompatibility, near-linear elasticity and large recoverable strain have been an important subject in the biomedical field [8−10].

It has been well recognized that when NiTi alloys exhibit pseudo-elastic deformation, they could show large recoverable strain originating from the stress-induced martensitic (SIM) transformation [11−14]. However, this type of large pseudo-elastic strain in the NiTi alloys is usually accompanied by visible stress-plateau on the stress−strain responses [11−13]. In the stress-plateau stage, the NiTi alloys are unable to bear

Corresponding author: Guang-lei LIU, Tel: +61-8-64888502, Fax: +61-8-64888502, E-mail: liugl@ujs.edu.cn;
Qing-kun MENG, Tel: +86-516-83591870, Fax: +86-516-83591979, E-mail: qkmeng@cumt.edu.cn;
Xin-qing ZHAO, Tel: +86-10-82338559, Fax: +86-10-82338200, E-mail: xinqing@buaa.edu.cn

DOI: 10.1016/S1003-6326(22)65970-3

effectively the external loads any longer [11−13], which is detrimental to practical applications. Antecedent studies suggested that the existence of stress-plateau in NiTi alloys is primarily due to a localized SIM transformation proceeding intensively over a small stress range [15−17]. And it is also shown that by introducing structural factors (including dislocations and grain refinement, etc.), the extent and stress range of SIM transformation in metallic materials can be tailored [18,19]. In this context, through tuning carefully the martensitic characteristics of NiTi alloys, the stress-plateau in NiTi alloys could disappear and the NiTi alloys might display a near-linear elastic deformation behavior.

Referring to the biocompatibility of NiTi alloys, some investigations revealed that the release of detrimental nickel ions from the surface of NiTi alloys might cause a series of health problems, e.g., allergy and carcinogenicity [20−22]. Recently, it has been reported that the biocompatibility of NiTi alloys can be effectively improved through cladding the NiTi alloys with non-cytotoxic alloy shells [23]. Based on the aforementioned design concept, quite recently, a shell−core Nb/NiTi composite possessing both good biocompatibility and high near-linear-elastic deformability (namely near-linear elasticity and large recoverable strain) was designed and fabricated [24]. Preliminary results suggest that the achievement of high near-linear-elastic deforming ability of this composite is closely related to severe deformation in hot pack-rolling, cold rolling and pre-straining treatment [24]. However, the deformation mechanisms in Nb/NiTi composite during the pre-straining process still remain unexplored, though clarifying this issue could provide valuable information for designing the metallic composites with near-linear elasticity as well as large recoverable strain for biomedical applications.

In this work, the mechanisms responsible for deformation behavior of Nb/NiTi composite during pre-straining were systematically studied by employing in-situ synchrotron X-ray diffraction, transmission electron microscopy and tensile test, with particular focus on clarifying the contribution of SIM transformation to the deformation behavior in Nb/NiTi composite.

2 Experimental

The starting materials employed in this study were Nb sheets of 200 μm in thickness and commercial $Ni_{50.3}Ti_{49.7}$ (at.%) plate of 5000 μm in thickness. Two Nb sheets (serving as external shell) and a NiTi plate (serving as internal core) were hot pack-rolled into a shell−core-structured composite plate of ~550 μm in thickness. Then, the composite plate was cold-rolled to a thickness of ~403 μm without any intermediate annealing.

The FEI Nova Nano 450 scanning electron microscope (SEM) equipped with the energy dispersive spectroscope (EDS) was employed to analyze the interface characteristics of Nb/NiTi composite. The microstructure of this composite was characterized using a FEI Tecnai F20 transmission electron microscope (TEM). The specimen of 25 mm in the gauge length and ~0.40 mm × 4.74 mm in the sectional dimension for tensile experiment was cut along the original rolling direction by employing electron discharge method. Tensile experiment was performed using an Instron-8801 mechanical testing machine (strain rate of 1×10^{-3} s^{-1}) complemented by a strain extensometer. In-situ synchrotron X-ray diffraction (SXRD) investigation during tensile loading−unloading was carried out at the 11-ID-C beam line of the Advanced Photon Source at Argonne National Laboratory in USA. The incident X-rays (λ=0.1173 Å) with a beam cross-section of 0.4 mm × 0.4 mm were used to capture two-dimensional (2-D) diffraction images. These 2-D diffraction images were recorded on a Perkin−Elmer detector and azimuthally integrated employing the Fit2D software to acquire one-dimensional (1-D) diffraction spectrograms, as described in detail in Ref. [25].

3 Results and discussion

3.1 Microstructures

Figure 1(a) displays the cross-sectional low-magnification backscattered electron (BSE) SEM image for Nb/NiTi specimen. It is observable that Nb/NiTi specimen performs a shell−core structure, consisting of the external Nb shell (~14 μm-thick) and the internal NiTi core (~375 μm-thick). The

high-magnification BSE-SEM image is displayed in Fig. 1(b), where the EDS elemental distribution map for Nb is shown as an insert. One can see that no apparent precipitates are noticed at the Nb/NiTi interfaces, which is similar with the case of a previously reported NiTi−Nb system [26]. This indicates that upon hot pack-rolling as well as cold-rolling, a well bonded metallurgical interface is formed in Nb/NiTi composite. Based on Fig. 1(a), the volume fractions of Nb and NiTi components can be determined to be 7% and 93%, respectively, implying that the mechanical behavior of Nb/NiTi composite depends largely on the dominant NiTi component due to its high volume fraction.

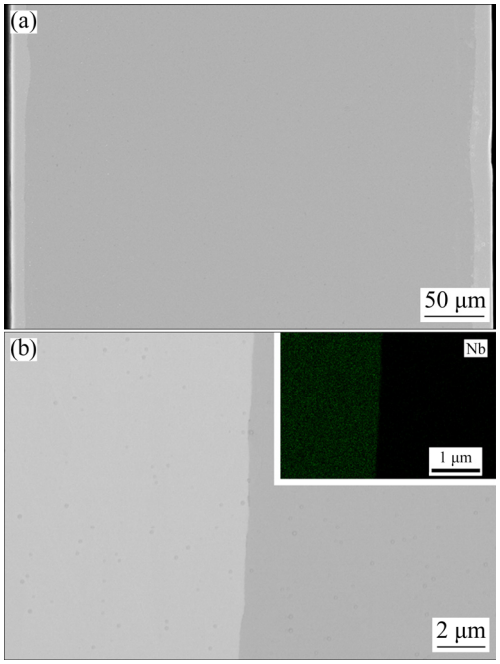

Fig. 1 Cross-sectional low-magnification (a) and high-magnification (b) backscattered electron (BSE) SEM images for Nb/NiTi specimen (The EDS elemental distribution map for Nb is shown as an insert)

Figure 2(a) shows the straightened Debye−Scherrer diffraction rings, where the diffraction rings corresponding to different crystal planes are indexed. It is clearly shown that diffraction rings from external Nb shell and internal NiTi core of Nb/NiTi specimen, including mainly $\{110\}_{\beta\text{-Nb}}$, $\{110\}_{B2}$ and $(001)_{B19'}$ diffraction rings, etc, are detected due to the large penetration depth and high resolution of the synchrotron X-ray diffraction (SXRD) technique [27−29]. Figure 2(b) shows the 1-D SXRD spectrogram for Nb/NiTi specimen. On the basis of the SXRD analysis, the phase composition of the Nb/NiTi specimen can be recognized as β-Nb phase, and $B19'$-NiTi phase along with a trace of $B2$-NiTi phase. Additionally, one can see that the $\{110\}_{B2}$ NiTi peak is much intenser than other B2-NiTi peaks, for example $\{100\}_{B2}$ and $\{200\}_{B2}$ peaks, suggesting that a $\langle 110\rangle_{B2}$ texture is prevalent in the present Nb/NiTi specimen. The presence of $\langle 110\rangle_{B2}$ texture can contribute to the external macroscopic deformation, because a large theoretical phase transformation strain can be generated through a $B2\rightarrow B19'$ stress-induced martensitic (SIM) transformation in the $B2$ texture [30].

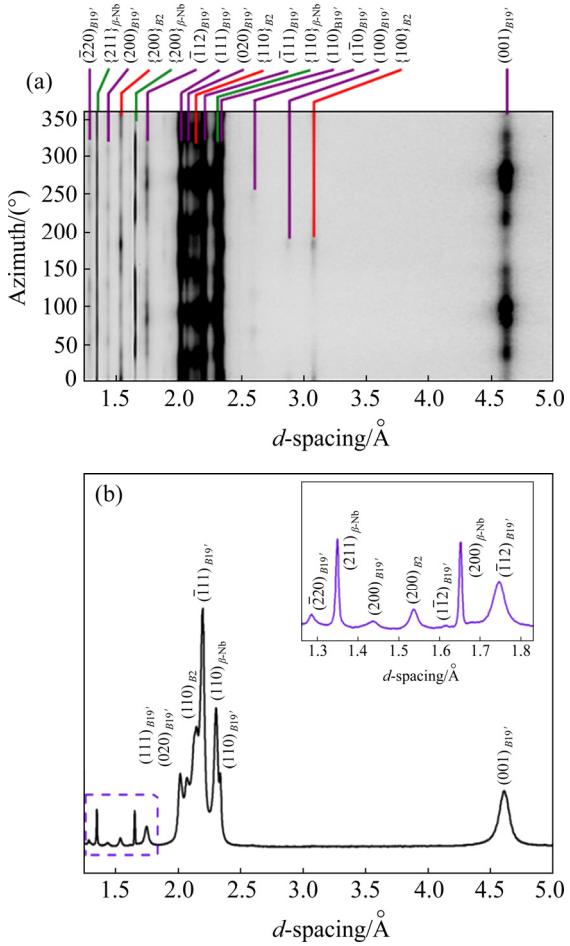

Fig. 2 Straightened Debye−Scherrer diffraction rings (a) and 1-D SXRD spectrogram (b) for Nb/NiTi specimen

Figure 3 displays the TEM micrographs of the internal NiTi core for Nb/NiTi specimen. From the bright-field micrograph displayed in Fig. 3(a), one can see that the NiTi exhibits a fine microstructure, where a number of dark areas generated by high-density dislocations can be seen. It is evident that the high-density dislocations are produced in the hot pack-rolling plus cold rolling process. This hot pack-rolling plus cold rolling process also

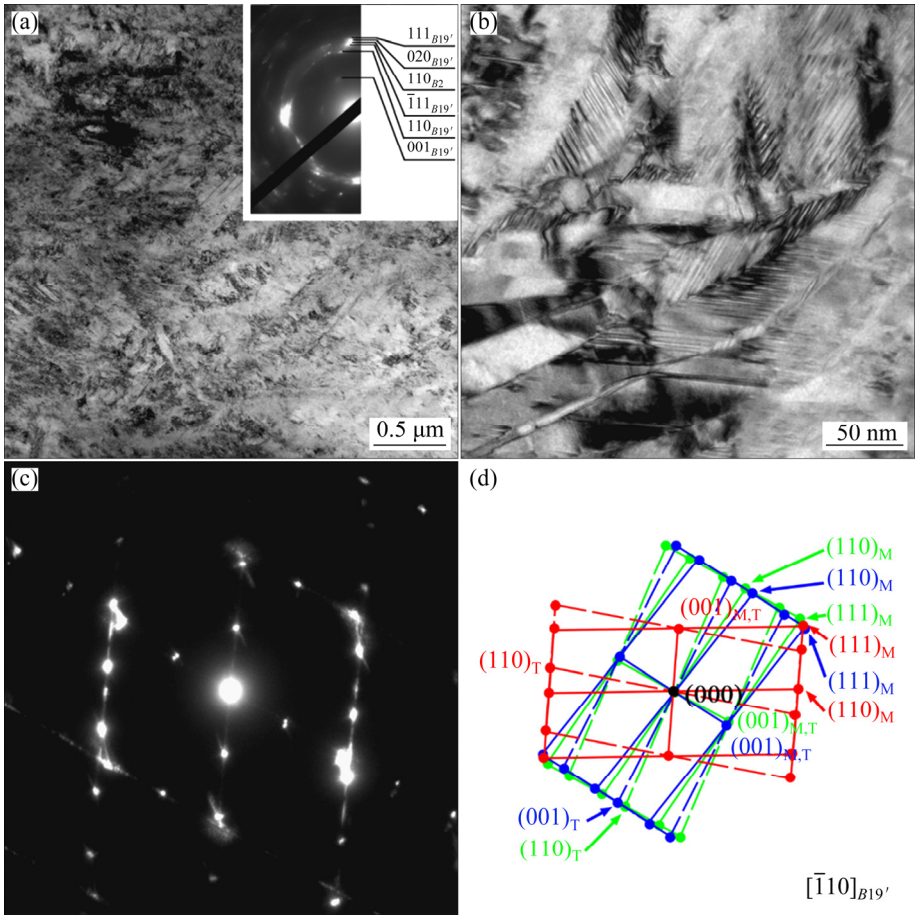

Fig. 3 TEM micrographs of internal NiTi core for Nb/NiTi specimen: (a) Bright-field micrograph and corresponding selected area diffraction pattern (SADP) (inset); (b) Higher-magnification bright-field micrograph; (c) SADP of (b); (d) Key diagram corresponding to SADP in (c)

results in remarkable grain refinement in the NiTi, which is verified by the roughly continuous diffraction rings in the selected area diffraction pattern (SADP, displayed as the insert at the upper right corner of Fig. 3(a)). Indexing of the SADP suggests that the NiTi is composed of *B*19′-phase and *B*2-phase, in accordance with the results of SXRD (Fig. 2). Figures 3(b, c) show the higher-magnification bright-field micrograph and the corresponding SADP of NiTi, respectively. It is observable from Fig. 3(b) that fine twins with different orientations are found in the *B*19′ martensite. Theses twins with different orientations give rise to the superimposition of several sets of diffraction patterns, as shown in Fig. 3(c). A careful analysis of SADP is shown in the key diagram in Fig. 3(d), where three sets of dots stemming from the matrices and twins are presented and marked by different colors. It is shown that the matrix and twin in every set of dots show mirror-symmetric relationship about the (001) plane of them, implying that the twinning relationship in *B*19′ martensite is in the (001) compound mode.

3.2 Mechanical properties

The macroscopic stress−strain curve for Nb/NiTi specimen under the tensile loading−unloading procedure (i.e., the pre-straining process) is represented in Fig. 4. It can be seen that during loading to 8.0% strain, there exists a remarkable change in the slope of the stress−strain curve at ~3.0% strain, indicated by the demarcation point in Fig. 4. Upon unloading, the macroscopic stress decreases linearly with decreasing macroscopic strain and then decreases nonlinearly, with a large recoverable strain of ~3.9%. During the subsequent heating to 423 K for 5 min, most of the residual unrecoverable macroscopic strain after unloading can be recovered (as shown by the dotted arrow), showing that the Nb/NiTi specimen possesses shape memory effect during heating.

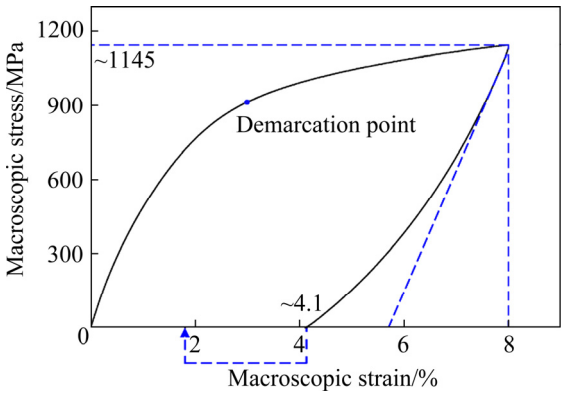

Fig. 4 Macroscopic stress−strain curve for Nb/NiTi specimen in tensile loading−unloading procedure (The dotted arrow indicates the recoverable macroscopic strain during heating)

3.3 In-situ synchrotron X-ray diffraction analysis

To explore the underlying mechanisms responsible for deformation behavior in Nb/NiTi specimen, the in-situ SXRD investigation was conducted on Nb/NiTi specimen. Figure 5 shows the variation in 1-D SXRD spectrograms for Nb/NiTi specimen corresponding to different strain levels in the tensile loading−unloading procedure. It can be seen that Nb/NiTi specimen experiences a *B*2↔*B*19′ stress-induced martensitic (SIM) transformation, which is verified by the progressive intensification of $(001)_{B19'}$ peak by consuming $\{200\}_{B2}$ peak upon loading and slight reduction of $(001)_{B19'}$ peak upon unloading. Additionally, it can be seen that upon loading, all the diffraction peaks move towards the right side (i.e., the larger *d*-spacing values), whereas upon unloading, these diffraction peaks shift to the left side (that is, the smaller *d*-spacing values). Clearly, the right shift of the diffraction peaks is due to the elastic elongation of Nb/NiTi specimen, while the left shift of the diffraction peaks is attributable to elastic recovery of the Nb/NiTi specimen.

The evolution in *d*-spacing for diffraction peaks for Nb/NiTi specimen with respect to macroscopic strain can be observed more clearly in Fig. 6, where isolated diffraction peaks stemming from *B*19′, *B*2 and *β*-Nb phases, including $(001)_{B19'}$, $\{200\}_{B2}$ and $\{200\}_{\beta\text{-Nb}}$ peaks, are chosen as targets to analyze in detail. As shown in Figs. 6(a, b), one can see that upon loading, the evolution in *d*-spacing of $(001)_{B19'}$ and $\{200\}_{B2}$ peaks can be divided into two stages. During loading in 0−3.0% macroscopic strain range, the *d*-spacing of $(001)_{B19'}$ and $\{200\}_{B2}$ peaks increases almost-monotonously and sharply with increasing macroscopic strain, showing that the *B*19′-phase and *B*2-phase are elongated elastically. With further loading to 8.0% strain, the *d*-spacing of $\{200\}_{B2}$ and $(001)_{B19'}$ peaks increases slightly, implying that besides the elastic

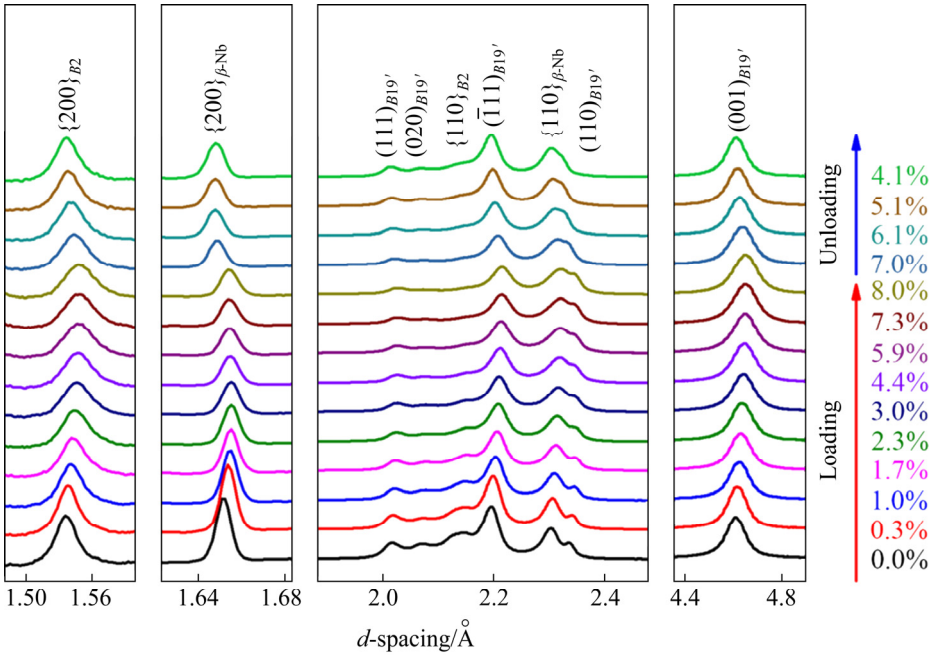

Fig. 5 Variation in 1-D SXRD spectrograms for Nb/NiTi specimen corresponding to different strain levels under tensile loading−unloading procedure

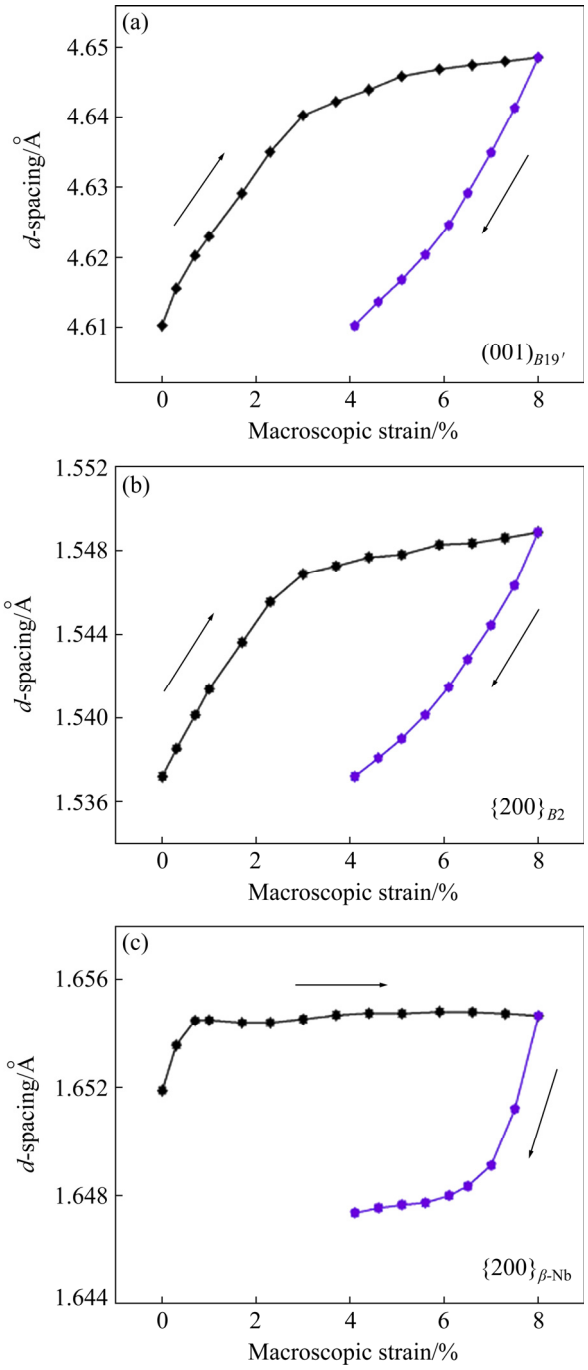

Fig. 6 Evolution in *d*-spacing for diffraction peaks stemming from *B*19′ (a), *B*2 (b) and *β*-Nb (c) phases for Nb/NiTi specimen with respect to macroscopic strain

elongation, the *B*2-phase and *B*19′-phase also undergo a forward *B*2→*B*19′ SIM transformation and a slight plastic deformation for the sake of accommodating macroscopic strain. Combining the results shown in Figs. 4, 6(a, b), one can see that the demarcation point on the macroscopic stress−strain curve (~3.0% strain point, Fig. 4) corresponds well to the critical point (~3.0% strain point) where the slope of *d*-spacing begins to change significantly in Figs. 6(a, b). Therefore, the presence of demarcation point in Fig. 4 can be reasonably ascribable to the *B*2→*B*19′ SIM transformation as well as the initiation of the slight plastic deformation of *B*19′-phase and *B*2-phase. During unloading, the *d*-spacing of $(001)_{B19'}$ and $\{200\}_{B2}$ reduces with reducing macroscopic strain and returns to their respective original values at a strain of 4.1%, revealing that an elastic recovery takes place in the *B*19′-phase and *B*2-phase of Nb/NiTi specimen.

Figure 6(c) displays the evolution in *d*-spacing for diffraction peak stemming from *β*-Nb phase with respect to macroscopic strain. It can be observed that during loading at strains below 1.0%, the *β*-Nb is elongated elastically, verified by the continuous increase in *d*-spacing of $\{200\}_{\beta\text{-Nb}}$ peak with the increment in macroscopic strain. Within the macroscopic strain range covering 1.0%−8.0%, the $\{200\}_{\beta\text{-Nb}}$ *d*-spacing stays approximately constant irrespective of the consecutively increasing macroscopic strain, indicating that a potential plastic deformation takes place in Nb layers. In the following unloading process, the $\{200\}_{\beta\text{-Nb}}$ *d*-spacing decreases with reducing macroscopic strain and the *β*-Nb experiences elastic recovery and the subsequent compressive deformation.

Figure 7 shows the evolution in integrated intensities for diffraction peaks stemming from *B*19′, *B*2 and *β*-Nb phases for Nb/NiTi specimen with respect to macroscopic strain. One can see from Figs. 7(a, b) that upon loading, $(001)_{B19'}$ and $\{200\}_{B2}$ exhibit a complementary intensity change, i.e., the increase in *B*19′-phase intensity and the reduction in *B*2-phase intensity. This indicates that the forward *B*2→*B*19′ SIM transformation takes place during loading. Upon unloading, with the reduction in macroscopic strain, the $(001)_{B19'}$ integrated intensity reduces (Fig. 7(a)), together with the intensification in $\{200\}_{B2}$ peak (Fig. 7(b)), signifying the occurrence of *B*19′→*B*2 reverse SIM transformation. Because of the existence of *B*19′→*B*2 reverse SIM transformation, the Nb/NiTi specimen recovers nonlinearly under unloading (Fig. 4). From Figs. 7(a, b), one can also see that the $(001)_{B19'}$ and $\{200\}_{B2}$ integrated intensities do not return to their respective original values, signifying that the reverse SIM transformation from *B*19′ to *B*2 is not completely reversible in the

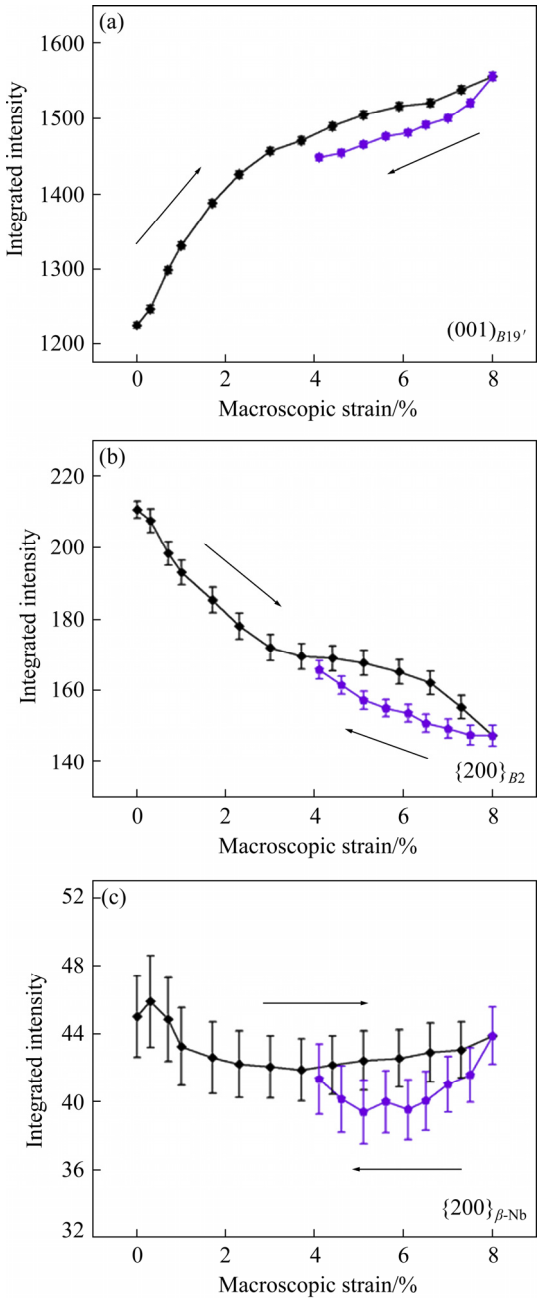

Fig. 7 Evolution in integrated intensities for diffraction peaks stemming from *B*19′ (a), *B*2 (b) and *β*-Nb (c) phases for Nb/NiTi specimen with respect to macroscopic strain

Nb/NiTi specimen. This incompletely reversible *B*2→*B*19′ SIM transformation, together with slight potential plastic deformation of *B*19′ and *B*2 phases (Fig. 6), can account for the residual macroscopic strain (~4.1%) of Nb/NiTi specimen after unloading (Fig. 4).

It is noteworthy that in the tensile loading−unloading procedure, the changes in the $(001)_{B19'}$ and $\{200\}_{B2}$ integrated intensities are consecutive and proceed over a wide range of stress (the whole tensile loading−unloading process, Figs. 4, 7(a, b)). The above results reflect a consecutive SIM transformation in Nb/NiTi specimen, in sharp contrast with localized SIM transformation taking place intensively in a small range of stress in conventional pseudo-elastic NiTi alloys [15,16]. This may be interpreted through considering the suppression effect of structural factors upon *B*2↔*B*19′ martensitic transformation. It has been well acknowledged that the shear and atomic shuffles are the intrinsic features of *B*2↔*B*19′ martensitic transformation [30], implying that some structural factors, e.g. dislocations and grain boundaries, could exert a significant effect on the suppression of *B*2↔*B*19′ martensitic transformation [31−33]. In the present study, the rolling process leads to the formation of high-density dislocations and grain boundaries in the internal NiTi (Fig. 3), which can obstruct the progress of shear and atomic shuffles indispensable for *B*2↔*B*19′ martensitic transformation, hence retarding the SIM transformation. Consequently, in Nb/NiTi specimen, a consecutive SIM transformation occurs throughout the tensile loading−unloading procedure.

As for the $\{200\}_{\beta\text{-Nb}}$ peak displayed in Fig. 7(c), it is seen that its intensity fluctuates slightly within the margin of error in the tensile loading−unloading procedure. This suggests that the Nb layers do not experience any visible solid phase transformation in the tensile loading−unloading procedure, which agrees well with the antecedent studies [34,35].

Figure 8 displays the straightened Debye−Scherrer diffraction rings of Nb/NiTi specimen under various strains in the tensile loading−unloading procedure, so that an intuitive demonstration with respect to the deformation behavior of Nb/NiTi specimen can be obtained. It is seen that the intensity of *B*19′ spots (labeled by purple arrows) intensifies gradually as macroscopic strain increases to 8.0%. At the same time, the intensity of *B*2 spots (labeled by red rectangles) weakens progressively with the increase in macroscopic strain. Upon unloading, the *B*19′ spots intensity weakens slightly, along with a slight intensification in *B*2 spots. These results signify that

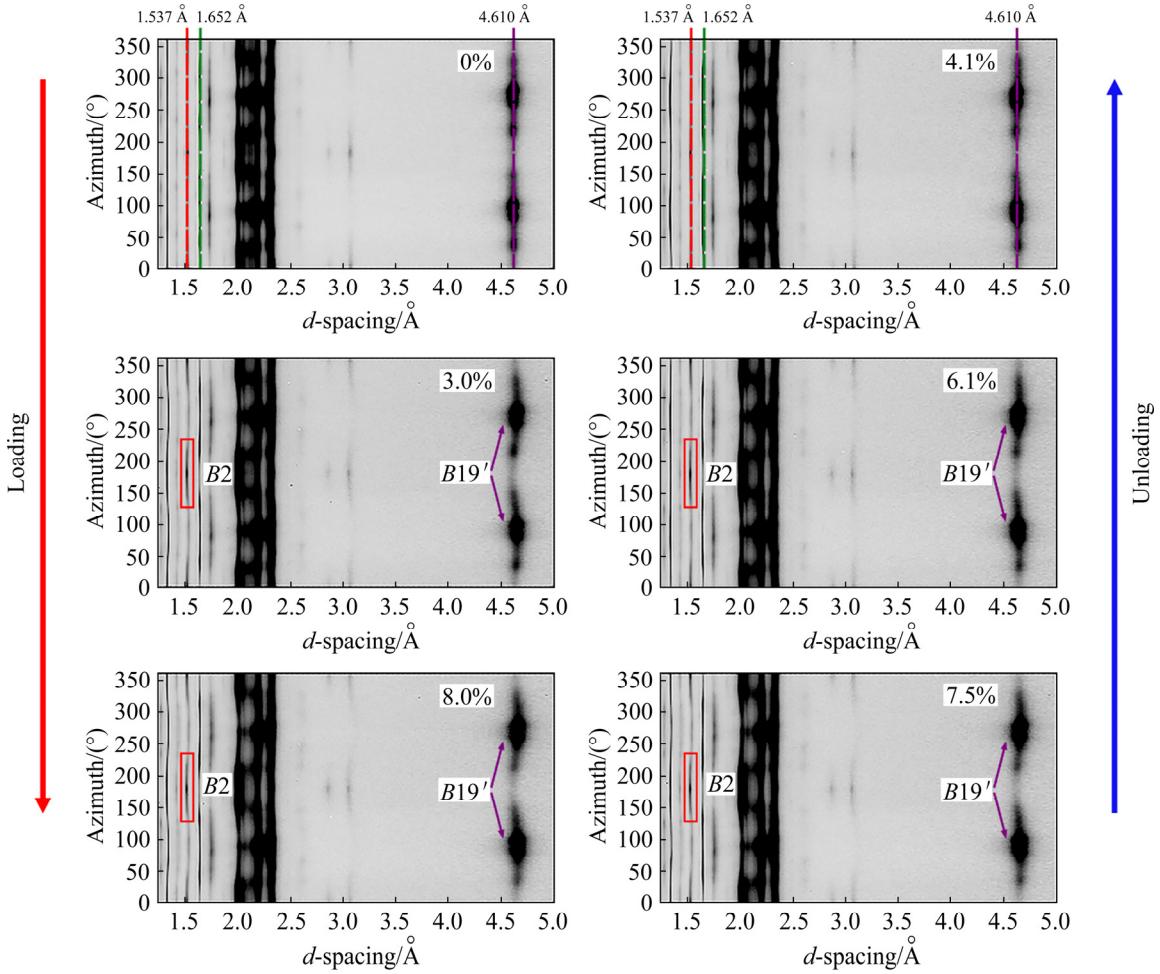

Fig. 8 Straightened Debye−Scherrer diffraction rings of Nb/NiTi specimen under various strains in tensile loading−unloading procedure (The initial positions (at 0% strain before loading) of $(001)_{B19'}$, $\{200\}_{B2}$ and $\{200\}_{\beta\text{-Nb}}$ diffraction rings are labeled by purple, red and green dashed lines, respectively)

Nb/NiTi specimen undergoes an incompletely reversible SIM transformation, in agreement with the results displayed in Fig. 7. Moreover, through a comparison between the diffraction rings before loading (at 0% strain) and those after unloading (at 4.1% strain), one can see that the positions of $(001)_{B19'}$ and $\{200\}_{B2}$ diffraction rings before loading are almost the same as those after unloading. The above result reveals that the internal NiTi layer does not retain remanent lattice strain after unloading. Unlike the internal NiTi layer, the external Nb layers persist a compressive strain after unloading, as verified by the fact that after unloading, the $\{200\}_{\beta\text{-Nb}}$ diffraction ring exhibits a slight left-shift from its initial position before loading (marked by green dashed lines).

From the aforementioned analyses, the zones of various deformation mechanisms in Nb/NiTi specimen in tensile loading−unloading procedure can be elucidated clearly, as shown in Fig. 9. During loading, the internal NiTi layer is elongated elastically in the 0−3.0% macroscopic strain range (Figs. 6(a, b)). Besides the elastic elongation, the internal NiTi layer also undergoes a slight plastic deformation in 3.0%−8.0% macroscopic strain range (Figs. 6(a, b)). Additionally, during the whole loading process, the internal NiTi layer experiences forward $B2 \rightarrow B19'$ SIM transformation (Figs. 7(a, b)). Upon the following unloading, the internal NiTi layer experiences a $B19' \rightarrow B2$ reverse SIM transformation (Figs. 7(a, b)) and elastic recovery (Figs. 6(a, b)). Referring to the external Nb layers, they undergo successively elastic elongation at macroscopic strains below 1.0% and plastic deformation in the 1.0%−8.0% macroscopic strain range (Fig. 6(c)) during loading. Upon the subsequent unloading, they first recover elastically and then experience compressive deformation with

further unloading (Fig. 6(c)). After unloading, the residual strain of ~4.1% in Nb/NiTi specimen is primarily ascribable to incompletely reversible SIM transformation from *B*2 to *B*19′ and the possible plastic deformation of the *B*19′ martensite, *B*2 and *β*-Nb phases (Figs. 6 and 7).

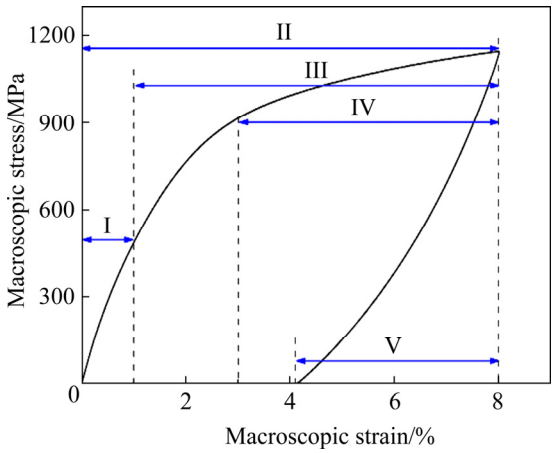

Fig. 9 Zones of various deformation mechanisms in Nb/NiTi specimen in tensile loading−unloading procedure (I—Elastic elongation of Nb; II—Elastic elongation of *B*19′ and *B*2, together with *B*2→*B*19′ SIM transformation; III—Tensile plastic deformation of Nb; IV—Tensile plastic deformation of *B*19′ and *B*2; V—Elastic recovery and compressive deformation of Nb, elastic recovery of *B*19′ and *B*2, together with *B*19′→*B*2 reverse SIM transformation)

Besides the above-mentioned inherent elastic deformation and SIM transformation, the (001) compound twins in *B*19′ martensite (Fig. 3) can also contribute to the elastic elongation and recovery occurring in *B*19′-phase of Nb/NiTi specimen. In fact, ZHENG et al [36] have reported that the (001) compound twins in the *B*19′ martensite can nucleate and grow upon loading and then shrink and disappear upon unloading, thus leading to the super-elastic deformation of NiTi alloy. Hence, it is reasonable to believe that the existence of (001) compound twins (Fig. 3) can also be helpful for elastic deformation occurring in *B*19′-phase of present Nb/NiTi specimen, similar to that in *B*19′-phase of NiTi [36].

4 Conclusions

(1) Under loading, the composite undergoes the elastic elongation and slight plastic deformation of *B*19′, *B*2 and *β*-Nb phases, along with forward stress-induced martensitic (SIM) transformation from *B*2 to *B*19′.

(2) During the unloading process, the deformation mechanisms in the composite primarily include the elastic recovery of *B*19′, *B*2 and *β*-Nb phases, and compression deformation of *β*-Nb phase coupled with incomplete *B*19′→*B*2 reverse SIM transformation.

(3) In the procedure of loading and unloading, in addition to the inherent elastic deformation and SIM transformation, the (001) compound twins in *B*19′ martensite can also be helpful for the elastic deformation taking place in the *B*19′-phase of the composite.

(4) The large recoverable strain of the composite after unloading is attributable to the inherent elastic deformation, and the incompletely reversible and consecutive SIM transformation coupled with the (001) compound twins in *B*19′ martensite.

Acknowledgments

The authors are grateful for the National Natural Science Foundation of China (Nos. 51771082, 51971009, 52175410, 51801076), the Six Talent Peaks Project in Jiangsu Province, China (No. 2019-XCL-113), Zhenjiang Science & Technology Program, China (No. GY2020001) and Project of Faculty of Agricultural Equipment of Jiangsu University, China (No. NZXB20200101). The authors also appreciate the US Department of Energy, Office of Science and Office of Basic Energy Science (No. DE-AC02-06CH11357) for providing the Advanced Photon Source.

References

[1] LI Jin-hua, WU Cheng-tie, CHU P K, GELINSKY M. 3D printing of hydrogels: Rational design strategies and emerging biomedical applications [J]. Materials Science and Engineering R, 2020, 140: 100543.

[2] PARK W, SHIN H, CHOI B, RHIM W K, NA K, HAN D K. Advanced hybrid nanomaterials for biomedical applications [J]. Progress in Materials Science, 2020, 114: 100686.

[3] MIHALCEA E, VERGARA-HERNÁNDEZ H J, JIMENEZ O, OLMOS L, CHÁVEZ J, ARTEAGA D. Design and characterization of Ti6Al4V/20CoCrMo-highly porous Ti6Al4V biomedical bilayer processed by powder metallurgy [J]. Transactions of Nonferrous Metals Society of China, 2021, 31: 178−192.

[4] PLAINE A H, da SILVA M R, BOLFARINI C. Tailoring the microstructure and mechanical properties of metastable

Ti−29Nb−13Ta−4.6Zr alloy for self-expansible stent applications [J]. Journal of Alloys and Compounds, 2019, 800: 35−40.

[5] NOLTEN U, KEMPF H, MATTES U, MOKWA W. Force sensor clip for orthopedic applications [J]. Procedia Engineering, 2010, 5: 730−733.

[6] OZAN S, LIN Ji-xing, LI Yun-cang, IPEK R, WEN C. Development of Ti−Nb−Zr alloys with high elastic admissible strain for temporary orthopedic devices [J]. Acta Biomaterialia, 2015, 20: 176−187.

[7] ZHANG G S, ZHANG Q, LI K F, CAO Y B, LI M, SHAN W K, GUO D F. Tailoring elastic admissible strain of TiZr alloy by cold rolling deformation [J]. Journal of Alloys and Compounds, 2019, 781: 504−507.

[8] TIAN Yu-xing, YU Zhen-tao, ONG C Y A, KENT D, WANG Gui. Microstructure, elastic deformation behavior and mechanical properties of biomedical β-type titanium alloy thin-tube used for stents [J]. Journal of the Mechanical Behavior of Biomedical Materials, 2015, 45: 132−141.

[9] ZHANG G S, ZHANG Q, LI K F, CAO Y B, LI M, SHAN W K, GUO D F. Tailoring elastic admissible strain of TiZr alloy by cold rolling deformation [J]. Journal of Alloys and Compounds, 2019, 781: 504−507.

[10] GORDIN D M, ION R, VASILESCU C, DROB S I, CIMPEAN A, GLORIANT T. Potentiality of the “Gum Metal” titanium-based alloy for biomedical applications [J]. Materials Science and Engineering C, 2014, 44: 362−370.

[11] WANG Xin-mei, XU Bao-xing, YUE Zhu-feng. Phase transformation behavior of pseudoelastic NiTi shape memory alloys under large strain [J]. Journal of Alloys and Compounds, 2008, 463: 417−422.

[12] SUN Fan, JORDAN L, da SILVA A, MARTIN F, PRIMA F. Revisiting the effects of low-concentration hydrogen in NiTi self-expandable stents [J]. Materials Science and Engineering C, 2021, 118: 111405.

[13] MOHAMMAD SHARIFI E, KERMANPUR A. Superelastic properties of nanocrystalline NiTi shape memory alloy produced by thermomechanical processing [J]. Transactions of Nonferrous Metals Society of China, 2018, 28: 515−523.

[14] ZHANG Pan-xin, ZHU Ming, WANG Le-you, LI Chong-he, ZHAI Qi-jie. Investigation on microstructure and memory property of NiTi single crystal shape memory alloys [J]. Rare Metal Materials and Engineering, 2010, 39: 762−766.

[15] SHAW J A, KYRIAKIDES S. On the nucleation and propagation of phase transformation fronts in a NiTi alloy [J]. Acta Materialia, 1997, 45: 683−700.

[16] NG K L, SUN Q P. Stress-induced phase transformation and detwinning in NiTi polycrystalline shape memory alloy tubes [J]. Mechanics of Materials, 2006, 38: 41−56.

[17] BAHADOR A, HAMZAH E, KONDOH K, ASMA ABUBAKAR T, YUSOF F, UMEDA J, SAUD S N, IBRAHIM M K. Microstructure and superelastic properties of free forged Ti−Ni shape-memory alloy [J]. Transactions of Nonferrous Metals Society of China, 2018, 28: 502−514.

[18] AHADI A, SUN Qing-ping. Stress-induced nanoscale phase transition in superelastic NiTi by in situ X-ray diffraction [J]. Acta Materialia, 2015, 90: 272−281.

[19] TSUCHIYA K, INUZUKA M, TOMUS D, HOSOKAWA A, NAKAYAMA H, MORII K, TODAKA Y, UMEMOTO M. Martensitic transformation in nanostructured TiNi shape memory alloy formed via severe plastic deformation [J]. Materials Science and Engineering A, 2006, 438/439/440: 643−648.

[20] POONKOTHAI M, VIJAYAVATHI B S. Nickel as an essential element and a toxicant [J]. International Journal of Environmental Sciences, 2012, 1: 285−288.

[21] KE Qing-dong, DAVIDSON T, KLUZ T, OLLER A, COSTA M. Fluorescent tracking of nickel ions in human cultured cells [J]. Toxicology and Applied Pharmacology, 2007, 219: 18−23.

[22] KASPRZAK K S, SALNIKOW K. Nickel toxicity and carcinogenesis [M]. New Jersey: John Wiley & Sons Ltd, 2007.

[23] GUO Shun, SHI Yu-lu, WU Rui-tang, LIU Hai-xia, MENG Qing-kun, LIU Guang-lei, CHENG Xiao-nong, ZHAO Xin-qing. Deformation behavior of a novel sandwich-like TiNb/NiTi composite with good biocompatibility and superelasticity [J]. Materials Science and Engineering A, 2020, 794: 139784.

[24] GUO Shun, ZHANG Hui-hui, CHEN Yue-liang, LIU Qing, WU Rui-tang, MA Wen, LIU Hai-xia, MENG Qing-kun, LIU Guang-lei, CHENG Xiao-nong, ZHAO Xin-qing. A sandwich-structured Nb/NiTi composite with good bio-compatibility, near-linear-elastic deformation and large elastic admissible strain [J]. Composites Part B, 2021, 207: 108586.

[25] ZHANG Jun-song, HAO Shi-jie, JIANG Da-qiang, HUAN Yong, CUI Li-shan, LIU Yi-nong, YANG Hong, REN Yang. In situ synchrotron high-energy X-ray diffraction study of microscopic deformation behavior of a hard-soft dual phase composite containing phase transforming matrix [J]. Acta Materialia, 2017, 130: 297−309.

[26] HAO Shi-jie, CUI Li-shan, JIANG Da-qiang, HAN Xiao-dong, REN Yang, JIANG Jiang, LIU Yi-nong, LIU Zhen-yang, MAO Sheng-cheng, WANG Yan-dong, LI Yan, REN Xiao-bing, DING Xiang-dong, WANG Shan, YU Cun, SHI Xiao-bin, DU Min-shu, YANG Feng, ZHENG Yanjun, ZHANG Ze, LI Xiao-dong, BROWN D E, LI Ju. A transforming metal nanocomposite with large elastic strain, low modulus, and high strength [J]. Science, 2013, 339(6124): 1191−1194.

[27] MENG Qing-kun, LI Huan, ZHAO Chong-hang, MA Wen, WEI Fu-xiang, SUI Yan-wei, QI Ji-qiu. Synchrotron X-ray diffraction characterization of phase transformations during thermomechanical processing of a Ti38Nb alloy [J]. Rare Metals, 2021, 40(11): 3269−3278.

[28] LI Shi-lei, WANG You-kang, CHE Zi-fan, LIU Gang, REN Yang, WANG Yan-dong. Investigations of deformation-induced $\delta\rightarrow\zeta$ phase transformation in zirconium hydride by in situ high-energy X-ray diffraction [J]. Acta Materialia, 2017, 140: 168−175.

[29] GUO Shun, WU Rui-tang, SHI Yu-lu, HOU Yan-pin, MA Wen, LIU Guang-lei, LIU Hai-xia, CHENG Xiao-nong. In situ synchrotron X-ray diffraction analysis of deformation behavior of a Nb/NiTi composite for biomedical applications [J]. Rare Metals, 2021, 40(3): 600−606.

[30] OTSUKA K, REN X. Physical metallurgy of Ti−Ni-based

shape memory alloys [J]. Progress in Materials Science, 2005, 50: 511−678.

[31] SHI X B, HU Z C, HU X W, ZHANG J S, CUI L S. Effect of plastic deformation on stress-induced martensitic transformation of nanocrystalline NiTi alloy [J]. Materials Characterization, 2017, 128: 184−188.

[32] ZHANG Hai-tian, LI Xiao-hong, ZHANG Xiang-yi. Grain-size-dependent martensitic transformation in bulk nanocrystalline TiNi under tensile deformation [J]. Journal of Alloys and Compounds, 2012, 544: 19−23.

[33] YANG Rui, MA Wei, WANG Chao, WANG Ting-mei, WANG Qi-hua. Effect of hot rolling on microstructure and tribology behaviors of Ti−50.8Ni alloy [J]. Transactions of Nonferrous Metals Society of China, 2021, 31: 967−979.

[34] JIANG H, BAARS D, ZAMIRI A, BIELER T R, BAUER P, COMPTON C, GRIMM T L. Mechanical properties of high RRR niobium with different texture [J]. IEEE Transactions on Applied Superconductivity, 2007, 17: 1291−1294.

[35] CROTEAU J F, PAI KULYADI E, KALE C, SIU D, KANG D, PEREZ FONTENLA A T, GARCíA-TABARéS VALDIVIESO E, BIELER T R, EISENLOHR P, SOLANKI K N, BALINT D, HOOPER P A, ATIEH S, JACQUES N, CANTERGIANI E. Effect of strain rate on tensile mechanical properties of high-purity niobium single crystals for SRF applications [J]. Materials Science and Engineering A, 2020, 797: 140258.

[36] ZHENG Y F, HUANG B M, ZHANG J X, ZHAO L C. The microstructure and linear superelasticity of cold-drawn TiNi alloy [J]. Materials Science and Engineering A, 2000, 279: 25−35.

Nb/NiTi 复合材料预变形过程中变形行为的原位同步辐射 X 射线衍射研究

郭 顺[1]，张慧慧[1]，Min-kyung KWAK[2]，丁 旺[1]，刘光磊[1]，马 雯[1,3]，刘海霞[1]，孟庆坤[4]，赵新青[5]

1. 江苏大学 材料科学与工程学院，镇江 212013；

2. Department of Materials Science and Engineering, Seoul National University, Seoul 08826, Korea；

3. 有研科技集团有限公司 有科期刊出版(北京)有限公司，北京 100088；

4. 中国矿业大学 材料科学与工程学院，徐州 221116；

5. 北京航空航天大学 材料科学与工程学院，北京 100191

摘 要：通过原位同步辐射 X 射线衍射、透射电子显微术和拉伸测试等表征手段，系统研究 Nb/NiTi 复合材料在预变形过程中的变形机制。结果表明：在加载过程中，Nb/NiTi 复合材料经历 *B*19′、*B*2 和 *β*-Nb 相的弹性伸长和轻微的塑性变形，以及从 *B*2 相到 *B*19′相的应力诱发马氏体相变。在随后的卸载过程中，Nb/NiTi 复合材料的变形机制主要包括 *B*19′、*B*2 和 *β*-Nb 相的弹性恢复，*β*-Nb 相的压缩变形以及不完全 *B*19′→*B*2 逆马氏体相变。在拉伸加载–卸载过程中，除了固有的弹性变形和应力诱发马氏体相变以外，复合材料中 *B*19′马氏体内部的(001)复合孪晶也有助于材料实现弹性变形。因此，由于弹性变形、部分可逆且“连续”的应力诱发马氏体相变以及(001)复合孪晶的共同作用，Nb/NiTi 复合材料在卸载完成后能够呈现出大的可恢复应变量。

关键词：Nb/NiTi 复合材料；近线性变形行为；大的可恢复应变量；马氏体相变

(Edited by Bing YANG)